



# JWST/MIRI Detection of Suprathermal OH Rotational Emissions: Probing the Dissociation of the Water by Ly $\alpha$ Photons near the Protostar HOPS 370

David A. Neufeld<sup>1</sup>, P. Manoj<sup>2</sup>, Himanshu Tyagi<sup>2</sup>, Mayank Narang<sup>2,3</sup>, Dan M. Watson<sup>4</sup>, S. Thomas Megeath<sup>5</sup>,  
Ewine F. Van Dishoeck<sup>6,7</sup>, Robert A. Gutermuth<sup>8</sup>, Thomas Stanke<sup>7</sup>, Yao-Lun Yang<sup>9</sup>, Adam E. Rubinstein<sup>4</sup>,  
Guillem Anglada<sup>10</sup>, Henrik Beuther<sup>11</sup>, Alessio Caratti o Garatti<sup>12</sup>, Neal J. Evans, II<sup>13</sup>, Samuel Federman<sup>5</sup>,  
William J. Fischer<sup>14</sup>, Joel Green<sup>14</sup>, Pamela Klaassen<sup>15</sup>, Leslie W. Looney<sup>16,17</sup>, Mayra Osorio<sup>10</sup>, Pooneh Nazari<sup>18</sup>,  
John J. Tobin<sup>17</sup>, Łukasz Tychoniec<sup>6</sup>, and Scott Wolk<sup>19</sup>

<sup>1</sup> William H. Miller III Department of Physics and Astronomy, The Johns Hopkins University, 3400 North Charles Street, Baltimore, MD, USA

<sup>2</sup> Department of Astronomy and Astrophysics, Tata Institute of Fundamental Research, Mumbai 400005, India

<sup>3</sup> Academia Sinica Institute of Astronomy & Astrophysics, Taipei 10617, Taiwan

<sup>4</sup> University of Rochester, Rochester, NY, USA

<sup>5</sup> University of Toledo, Toledo, OH, USA

<sup>6</sup> Leiden Observatory, Leiden University, P.O. Box 9513, 2300 RA Leiden, The Netherlands

<sup>7</sup> Max-Planck Institut für Extraterrestrische Physik, Garching bei München, Germany

<sup>8</sup> University of Massachusetts Amherst, Amherst, MA 01003, USA

<sup>9</sup> Star and Planet Formation Laboratory, RIKEN Cluster for Pioneering Research, Wako, Saitama 351-0198, Japan

<sup>10</sup> Instituto de Astrofísica de Andalucía, CSIC, Glorieta de la Astronomía s/n, E-18008 Granada, ES, Spain

<sup>11</sup> Max Planck Institute for Astronomy, Heidelberg, Baden Wuerttemberg, Germany

<sup>12</sup> INAF-Osservatorio Astronomico di Capodimonte, Italy

<sup>13</sup> Department of Astronomy, The University of Texas at Austin, Austin, TX 78712, USA

<sup>14</sup> Space Telescope Science Institute, 3700 San Martin Drive, Baltimore, MD 21218, USA

<sup>15</sup> United Kingdom Astronomy Technology Centre, Edinburgh, UK

<sup>16</sup> Department of Astronomy, University of Illinois, 1002 West Green Street, Urbana, IL 61801, USA

<sup>17</sup> National Radio Astronomy Observatory, 520 Edgemont Road, Charlottesville, VA 22903, USA

<sup>18</sup> European Southern Observatory, Karl-Schwarzschild-Strasse 2, 85748 Garching, Germany

<sup>19</sup> Center for Astrophysics Harvard & Smithsonian, Cambridge, MA, USA

Received 2024 February 8; revised 2024 March 19; accepted 2024 April 10; published 2024 May 1

## Abstract

Using the MIRI medium-resolution spectrometer on JWST, we have detected pure rotational, suprathermal OH emissions from the vicinity of the intermediate-mass protostar HOPS 370 (OMC2/FIR3). These emissions are observed from shocked knots in a jet/outflow and originate in states of rotational quantum number as high as 46 that possess excitation energies as large as  $E_U/k = 4.65 \times 10^4$  K. The relative strengths of the observed OH lines provide a powerful diagnostic of the ultraviolet radiation field in a heavily extinguished region ( $A_V \sim 10\text{--}20$ ) where direct UV observations are impossible. To high precision, the OH line strengths are consistent with a picture in which the suprathermal OH states are populated following the photodissociation of water in its  $\tilde{B} - X$  band by ultraviolet radiation produced by fast ( $\sim 80$  km s<sup>-1</sup>) shocks along the jet. The observed dominance of emission from symmetric ( $A'$ ) OH states over that from antisymmetric ( $A''$ ) states provides a distinctive signature of this particular population mechanism. Moreover, the variation of intensity with rotational quantum number suggests specifically that Ly $\alpha$  radiation is responsible for the photodissociation of water, an alternative model with photodissociation by a  $10^4$  K blackbody being disfavored at a high level of significance. Using measurements of the Br $\alpha$  flux to estimate the Ly $\alpha$  production rate, we find that  $\sim 4\%$  of the Ly $\alpha$  photons are absorbed by water. Combined with direct measurements of water emissions in the  $\nu_2 = 1 - 0$  band, the OH observations promise to provide key constraints on future models for the diffusion of Ly $\alpha$  photons in the vicinity of a shock front.

*Unified Astronomy Thesaurus concepts:* Protostars (1302); Infrared astronomy (786); Molecular gas (1073)

## 1. Introduction

In the realm of molecular astrophysics, one of the most remarkable results obtained by Spitzer was the detection of highly suprathermal OH rotational emissions. The observed transitions, detected with the Short-Hi module of the Infrared Spectrometer (IRS) toward the Herbig–Haro object HH 211 (Tappe et al. 2008), originate in pure rotational states with rotational quantum numbers  $N$  as high as 34 and energies as high as  $E/k = 2.8 \times 10^4$  K. They are naturally explained as

the “prompt emission” that follows the photodissociation of water via the  $\tilde{B} - X$  band (also known as the “second absorption band”) by radiation in the 114–134 nm wavelength range; this spectral region includes the strong Ly $\alpha$  line emitted by fast interstellar shocks. This explanation is supported by both laboratory and theoretical studies of water photodissociation through the  $\tilde{B} - X$  band, which indicate that OH states as high as  $N = 47$  can be populated (Harich et al. 2000; van Harrevelt & van Hemert 2000). Suprathermal OH emissions resulting from the photodissociation of water were subsequently observed in protostellar disks with Spitzer: the protostellar disk of DG Tau, in particular, has been the subject of a detailed analysis by Carr & Najita (2014).



Original content from this work may be used under the terms of the [Creative Commons Attribution 4.0 licence](https://creativecommons.org/licenses/by/4.0/). Any further distribution of this work must maintain attribution to the author(s) and the title of the work, journal citation and DOI.

Spitzer could not perform high-spectral-resolution observations shortward of  $10\ \mu\text{m}$ , the short-wavelength cutoff of the Short-Hi module of the IRS, and at shorter wavelengths, the Short-Lo module on Spitzer/IRS provided a spectral resolving power,  $\lambda/\Delta\lambda$ , of only  $\sim 60$ , which was insufficient to detect suprathermal OH emissions. By contrast, the MIRI medium-resolution spectrometer (MRS) on JWST provides coverage down to the OH band-head at  $9.13\ \mu\text{m}$  (and below), yielding spectra with a spectral resolving power of  $\sim 3000$ . This unique capability opens up the possibility of detecting suprathermal OH emission in the  $9\text{--}10\ \mu\text{m}$  range, a possibility that has been realized in observations of the Orion Bar reported very recently (Zannese et al. 2024), providing a powerful test of model predictions for the spectrum of the OH prompt emission (e.g., Tabone et al. 2021, hereafter T21).

In this Letter, we discuss JWST/MIRI observations of suprathermal OH emissions in the vicinity of the protostar HOPS 370. HOPS 370, aka OMC2/FIR3, is an intermediate-mass class 0/I protostar (Furlan et al. 2016). It is located north of the Orion Nebula in the OMC2 region of the integral-shaped filament at an estimated distance of 392 pc (Kounkel et al. 2018; Tobin et al. 2020, hereafter T20). Its central protostellar mass, determined from Keplerian motions, is  $2.5 M_{\odot}$ , and its bolometric luminosity is  $314 L_{\odot}$  (T20). Extensive observations of HOPS 370 have been carried out with multiple observatories—including Herschel, SOFIA, the Very Large Array, the Atacama Large Millimeter/submillimeter Array (ALMA), and now JWST—and together reveal an actively accreting protostar with a bipolar jet/outflow that is orthogonal to a rotating disk of estimated mass  $0.05\text{--}0.1 M_{\odot}$ . It powers a large outflow traced in millimeter and far-IR lines, which suggests that it is in a state of rapid accretion (Manoj et al. 2013; González-García et al. 2016; T20; Sato et al. 2023). This outflow consists of both a wide-angle wind and a collimated jet, the latter containing shocks that are also seen in nonthermal radio emission (Osorio et al. 2017). The orientation of the disk, with an estimated radius of 100 au, indicates that this source is observed at a high inclination angle of  $\sim 72^{\circ}$  (T20; Federman et al. 2023, and references therein). Luminous shocked knots in the northern outflow lobe are characterized by strong emissions from a variety of molecules and atomic ions detected in our observations, including  $\text{H}_2$ ,  $\text{H}_2\text{O}$ , CO, OH,  $\text{Fe}^+$ , and  $\text{Ne}^+$ .

In Section 2, we discuss the MIRI and NIRSpec observations carried out toward HOPS 370 and the methods used to reduce the data. The resultant spectra and spectral line maps are presented in Section 3, with particular emphasis on the suprathermal OH emissions from the shocked knots. The origin of those emissions is discussed in Section 4, in the context of a model in which water is photodissociated by shock-produced  $\text{Ly}\alpha$  radiation. A brief summary follows in Section 5.

## 2. Observations and Data Reduction

The observations of HOPS 370 were performed as part of the Cycle 1 medium GO program “Investigating Protostellar Accretion (IPA)” (PID 1802; Megeath et al. 2021), which carried out NIRSpec and MIRI integral field unit (IFU) observations toward five protostars spanning 5 orders of magnitude in luminosity (see Federman et al. 2023). A set of  $2 \times 2$  mosaics was obtained with NIRSpec using the G395M/F290LP disperser–filter combination, which provides coverage of the  $2.87\text{--}5.10\ \mu\text{m}$  spectral region at a spectral resolving

power of  $\lambda/\Delta\lambda \sim 1000$ , and with all channels of the MIRI/MRS to provide complete mid-infrared coverage from  $4.9$  to  $27.9\ \mu\text{m}$  at a spectral resolving power that ranged from 1500 to 4000 (Jones et al. 2023). The mosaicking was performed with a 10% overlap and a four-point dither pattern. The total observing time was about 7.5 hr, including overheads. Further details of the observing strategy have been presented by Federman et al. (2023) and Narang et al. (2024).

For the reduction of NIRSpec IFU data, we utilized JWST pipeline version 1.9.5 and the JWST Calibration References Data System (CRDS) context version `jwst_1069.pmap`. In our analysis, we identified hot pixels not captured by the JWST outlier detection step by applying a custom outlier detection algorithm specific to NIRSpec observations. More information on the NIRSpec data reduction and the custom flagging routine can be found in Federman et al. (2023).

The MIRI/MRS data reduction utilized JWST pipeline version 1.12.5 along with JWST CRDS context version `jwst_1179.pmap`. We used the standard Stage 1 JWST pipeline *Detector1Pipeline* to reduce the MIRI/MRS data starting from *uncal* data.

In the subsequent Stage 2 (*Spec2Pipeline*), we performed pixel-by-pixel background subtraction using dedicated background observations. This process effectively removed all identified bad pixels, resulting in background-subtracted *cal* products. However, we observed extended  $\text{H}_2\ \text{S}(1)$  and  $\text{H}_2\ \text{S}(2)$  emissions in the dedicated background observations, which led to reduced flux for these lines in the final data. Consequently, we repeated the *Spec2Pipeline* without background subtraction. In this case, we encountered hot pixels in the detector data, which we removed using the *VIP* package (Gomez Gonzalez et al. 2017; Christiaens et al. 2023). Furthermore, we performed residual fringe correction during Stage 2 for both scenarios, with and without background subtraction.

In Stage 3 (*Spec3Pipeline*), the *CubeBuildStep* was set to *band* mode, generating separate FITS files for each channel and band. We also generated data cubes without dedicated background subtraction, with the outlier rejection function turned off in these cases.

We measured and applied an astrometric offset calibration to the NIRSpec and MIRI IFU data to improve feature alignment and link the coordinates to the Gaia DR3 standard. The offset measurement process and listed offsets applied with uncertainties are presented in Federman et al. (2023).

Additional data reduction tasks were performed using a suite of Python scripts we developed to (1) extract spectra within a circular region of any specified position and radius, (2) fit and subtract a continuum from the extracted spectra, (3a) fit Gaussian lines to continuum-subtracted spectra obtained from task 2 above, or (3b) fit Gaussian lines with a first-order baseline at each IFU position and for each spectral line we targeted, thereby enabling us to generate spectral line maps.

The second of these tasks (continuum fitting) was accomplished using a procedure that lacked any knowledge of the wavelengths of expected spectral lines. This “zero-knowledge” feature avoids the risk of artificially creating spectral lines where lines are expected. Here, for each spectral channel, we fit a third-order polynomial to the fluxes measured within a 17-channel window centered on that spectral channel (i.e., with eight spectral channels on either side of the central one). The fit was optimized to achieve the best fit to any 10 of the 17 spectral channels in the window, and the continuum flux value

for the central channel was then assigned in accordance with that fit. For spectral regions where lines cover less than  $7/17 \sim 40\%$  of the spectral samples, this procedure yields a reliable separation of the continuum (including instrumental baseline ripples) from the lines. For the third task, Gaussian fitting, we used the Levenberg–Marquardt algorithm; here, the line centroid and width were allowed to vary over a narrow range and the line intensity was allowed to vary freely, as were the continuum level and slope for task 3b.

### 3. Results

The IFU data acquired toward HOPS 370 are extraordinarily rich, revealing literally hundreds of spectral lines with a signal-to-noise ratio adequate for mapping. These data have and will be presented and discussed in a series of papers, some already published (Federman et al. 2023; Rubinstein et al. 2023; Brunken et al. 2024; Nazari et al. 2024) and some in preparation. Here, we focus on the suprathermal OH lines and a small set of ancillary lines that are directly relevant to their interpretation.

#### 3.1. Spectral Line Maps

In Figure 1, we present maps of several spectral lines: a strong well-isolated water line within the  $\nu_2 = 1 - 0$  vibrational band; the average of nine pure rotational lines of OH, with upper states with  $N_U$  between 34 and 43<sup>20</sup>; the Br $\alpha$  line at  $4.05 \mu\text{m}$ , which traces the Ly $\alpha$  radiation responsible for the photo-dissociation of water to produce suprathermal OH emissions; the  $\nu = 0 - 0$  S(3) line of H<sub>2</sub> at  $9.66 \mu\text{m}$ , one of eight pure rotational lines detected with MIRI/MRS that may be used to estimate the extinction toward the source; the [Fe II]  $5.34 \mu\text{m}$  line, a transition recently shown by Narang et al. (2024) to be an excellent tracer of collimated jets in another IPA target source, IRAS 16253–2429; and the [Ne II]  $12.81 \mu\text{m}$  line, a signature of fast, ionizing shocks. The maps are masked in the vicinity of a bright continuum source in the south, MIPS 2301 (Megeath et al. 2012), where the line fits are unreliable. The R.A. and decl. offsets are given in arcseconds relative to the ALMA source position (T20; green star): R.A. =  $83^\circ.865142$ , decl. =  $-5^\circ.159561$  (J2000).

Red circles near the lower right of each panel indicate the half-power beam width (HPBW) at the relevant wavelength, as determined by the linear fit given by Law et al. (2023). All these emissions peak roughly  $0''.8$  north of the ALMA source position, near the location of the shocked knots identified by Federman et al. (2023). The maps presented in Figure 1 exhibit a remarkable dynamic range: they are shown with a logarithmic stretch extending down to 0.1% of the peak intensity. In units of  $10^{-4} \text{ erg cm}^{-2} \text{ s}^{-1} \text{ sr}^{-1}$ , the peak velocity-integrated line intensities are 73, 1.14, 12.7, 36, 67, and 60, respectively, for the H<sub>2</sub>O, OH, Br $\alpha$ , H<sub>2</sub>, [Fe II], and [Ne II] lines. For all the mapped lines other than the suprathermal OH emissions, a line is securely detected in every spaxel right up to the edges of the mapped region. While the [Fe II] and [Ne II] fine-structure emissions primarily trace a collimated bipolar jet, the H<sub>2</sub> emissions are much less strongly collimated (Federman et al. 2023) and appear to trace a wide-angle wind. The Br $\alpha$ , OH, and H<sub>2</sub>O emissions show an intermediate degree of collimation. Velocity shifts, although smaller than the instrumental line

widths, are clearly detected and indicate that the northern jet is tilted toward us and the southern jet away from us. They will be the subject of a future study.

#### 3.2. OH Suprathermal Emission Spectra

In Figure 2, we present the  $8.8\text{--}13.4 \mu\text{m}$  spectra obtained toward the shocked knots within the circular region indicated by the white circle in Figure 1. This aperture has a radius of  $0''.8$  and is centered at a projected distance of 316 au from the protostar (ALMA position) on the OH emission peak at offset  $(\Delta\alpha \cos \delta, \Delta\delta) = (+0''.1, +0''.8)$ . The spectral region shown in Figure 2 covers 24 securely detected lines of OH, originating in states with  $N_U$  ranging from 23 to 46, along with five fine-structure lines of [Ni II], [Co II], [Cl I], and [Ne II] and two pure rotational lines of H<sub>2</sub>, S(2) and S(3).

From top to bottom, separate panels show the observed MIRI Band 2B (Channel 2 subband B) spectrum, with the continuum fit (blue) obtained using the procedure for task 2 described in Section 2 above, and the continuum-subtracted Band 2B, 2C, and 3A spectra. Colored vertical lines at the bottom of the lower three panels show the positions of suprathermal OH lines (Brooke et al. 2016), following the color coding indicated in the second panel from the top. Each rotational transition  $N \rightarrow N - 1$  is split into a quartet of lines by the combined effects of lambda-doubling and spin-orbit coupling, and the four lines are spectrally resolvable by MIRI/MRS except at the highest values of  $N$ .

Two of the four transitions connect so-called  $A'$  states, which are symmetric with respect to reflection about the plane of rotation of the molecule, and two connect antisymmetric  $A''$  states. (A further hyperfine splitting associated with the nuclear spin of H cannot be resolved spectrally with MIRI/MRS for any of the observed transitions.) The observed emission is completely dominated by intraladder transitions involving symmetric  $A'$  states of OH (i.e., the lower  $e$  lambda doublets of the  ${}^2\Pi_{3/2}$  ladder and the lower  $f$  lambda doublets of the  ${}^2\Pi_{1/2}$  ladder, shown with green and red lines.)

In Figure 3, we show zoomed spectra of the suprathermal OH lines (yellow histogram). Here, the black lines show Gaussian fits to each line. These were obtained with the central wavelengths allowed to vary over a narrow range but with the wavelength separation of the two components fixed at the laboratory value and the flux ratio of the two components fixed at unity. The velocity scale is referenced to the average wavelength of the two components. At the spectral resolution of MIRI, the separation of the  ${}^2\Pi_{3/2}(e)$  and  ${}^2\Pi_{1/2}(f)$  transitions is unresolved for the highest- $N_U$  lines detected and fully resolved for  $N_U \leq 23$ . Line positions are marked with vertical lines for each component of the OH quartet, with the same color coding as in Figure 2: only the  $A'$  states (red and green) are detected. Some transitions with  $N_U < 20$  are detected, but most lie in spectral regions where flux measurements are unreliable due to instrumental fringing. They are not plotted here, and their fluxes are not used in the analysis presented in Section 4.1 below.

#### 3.3. H<sub>2</sub> Rotational Diagram and Inferred Extinction

While the H<sub>2</sub> emissions from HOPS 370 will be discussed in detail in a future publication, their present relevance is simply in providing a valuable extinction estimate. Their usefulness for this purpose arises because the S(3) line lies close to a local

<sup>20</sup> Here, we excluded the OH  $N = 37 - 36$  line, which lies very close to the much stronger S(3) line of H<sub>2</sub>.

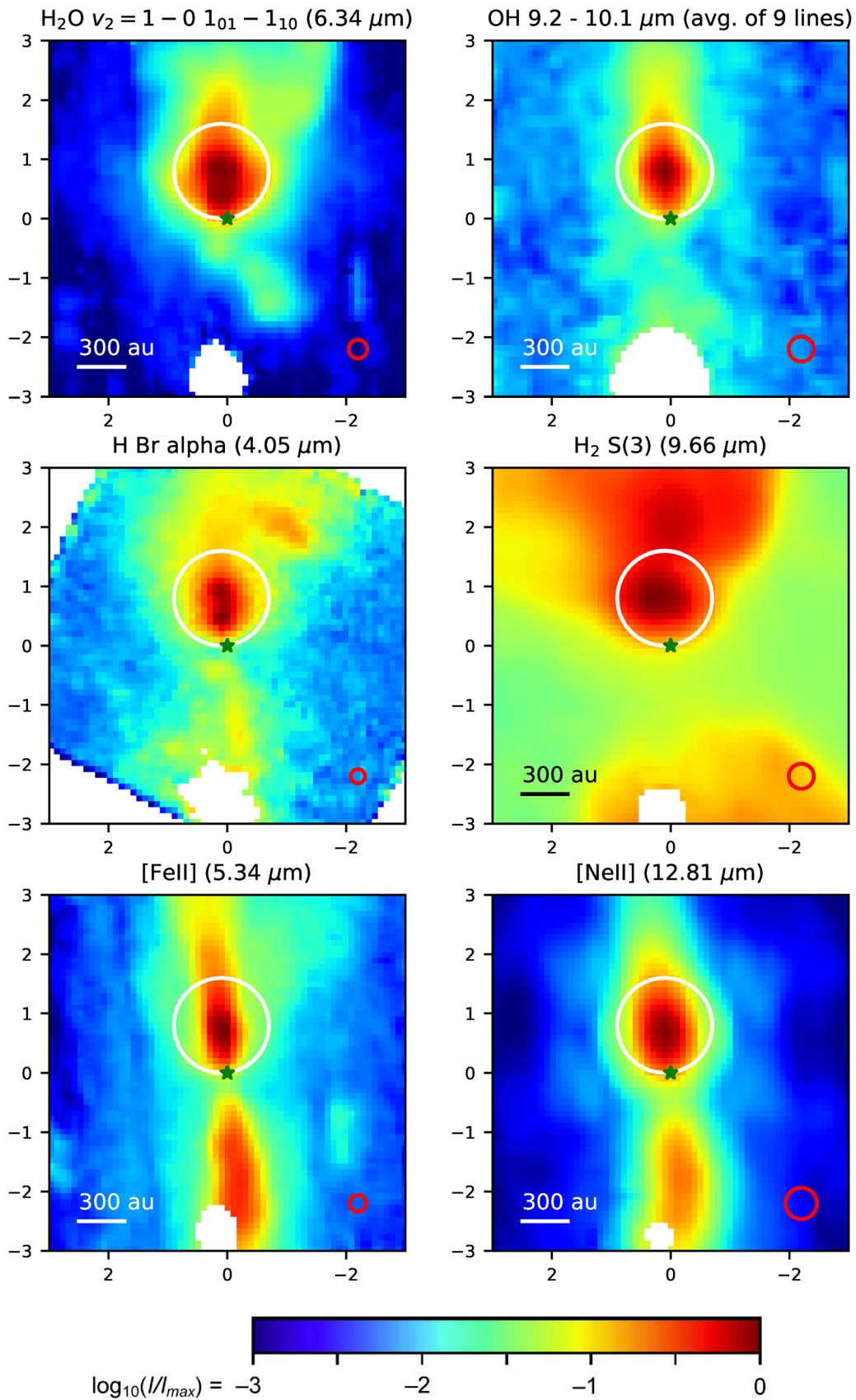


**Figure 1.** Spectral line maps obtained toward HOPS 370, shown with a logarithmic stretch. R.A. and decl. offsets are given in arcseconds relative to the ALMA source position (green star). The white circle demarks a  $0''.8$  radius region centered on the shocked knot. The maps are masked near a bright continuum source in the south where the line fits are unreliable. The red circles show the beam size (HPBW).

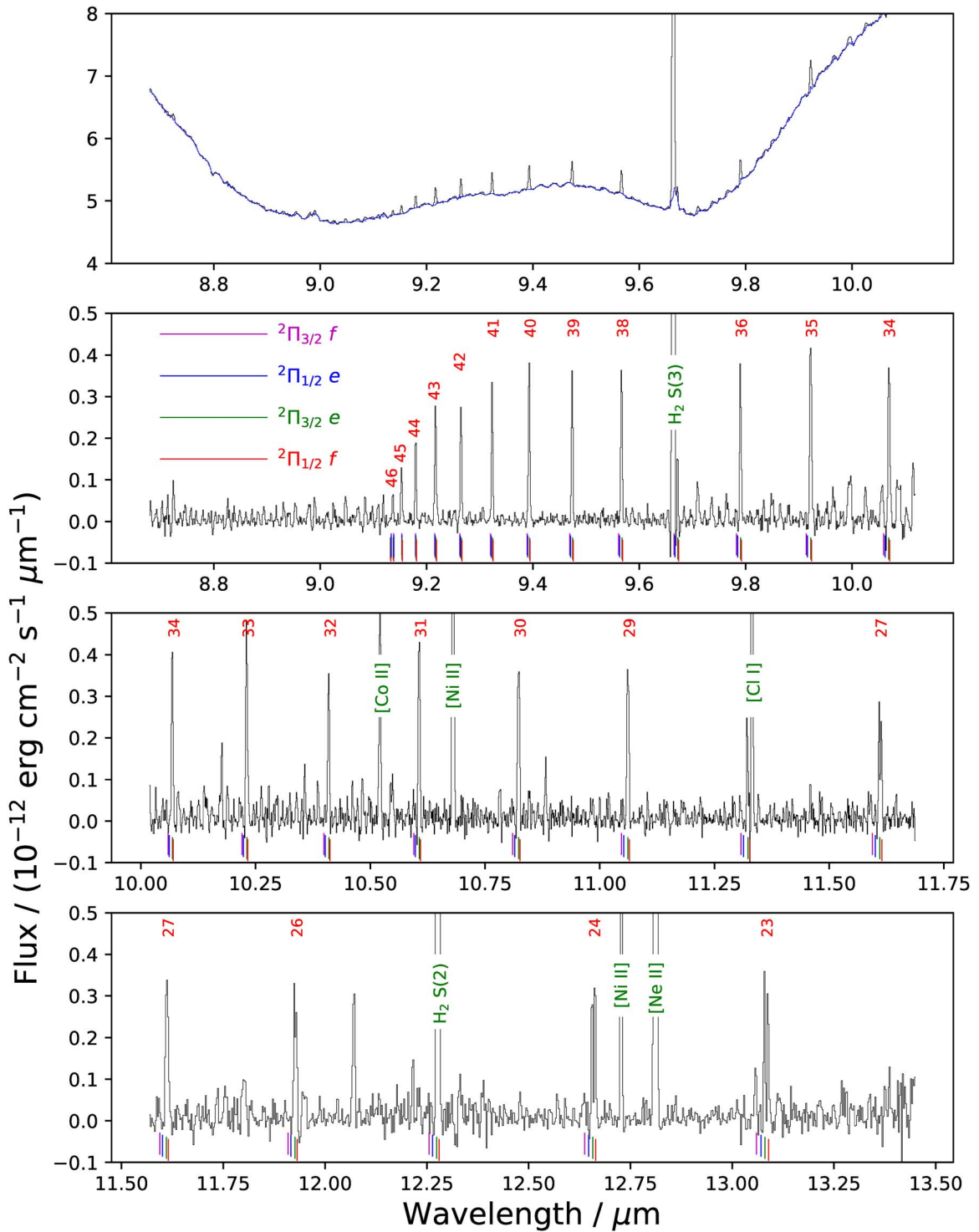


**Figure 2.** The 8.8–13.4  $\mu\text{m}$  spectra obtained toward the shocked knots. From top to bottom: Band 2B spectrum with continuum fit in blue; continuum-subtracted Band 2B, 2C, and 3A spectra. Red numbers above the OH lines indicate the value of  $N_U$ .

maximum in the extinction curve—associated with the silicate absorption feature—and therefore provides excellent leverage on the line-of-sight extinction. Using the intensities of the S(1)–S(8) pure rotational lines of  $\text{H}_2$  measured with MIRI/MRS, we constructed the rotational diagram shown in Figure 4. Here, we convolved the S(2)–S(8) MIRI maps with 2D Gaussian kernels of the widths needed to degrade the spatial resolution to a common value for all lines. We then obtained

average intensities for each line within the circular aperture indicated by the white circle in Figure 1.

Following Neufeld et al. (2006), for example, we fit the rotational diagram with the sum of two components each in local thermodynamic equilibrium (LTE): a warm component at temperature  $T_w$ , with an aperture-averaged column density,  $N_w$ ; and a hot component at temperature  $T_h$ , with an aperture-averaged column density,  $N_h$ . These components were allowed

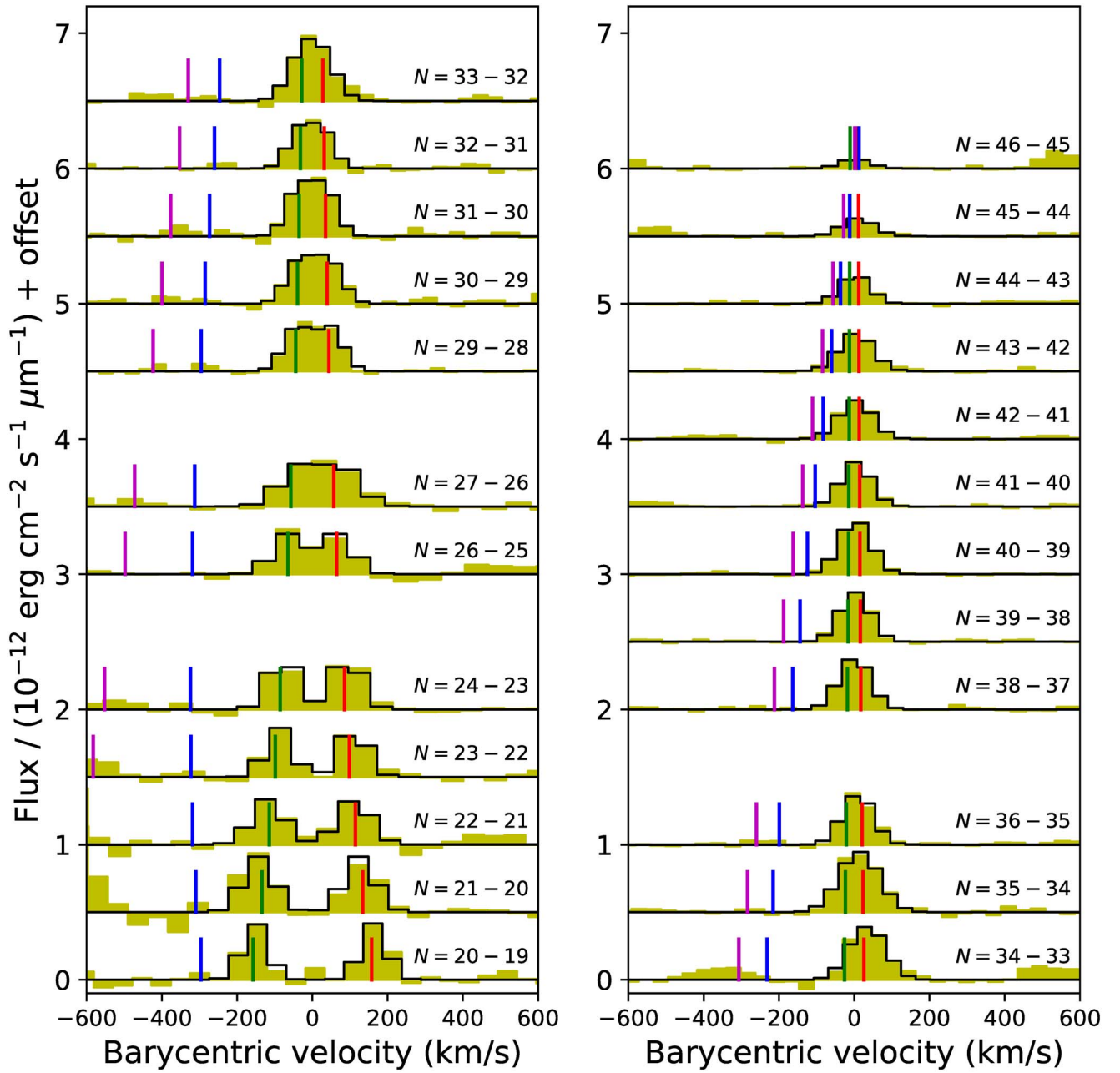


**Figure 3.** Spectra of suprathermal OH lines observed toward the shocked knots. Yellow: observed spectrum. Line positions are marked with vertical lines for each component of the OH quartet, with the same color coding as in Figure 2. Black histogram: Gaussian fit to the A' components (see text).

to have separate ortho-to-para ratios,  $\text{OPR}_w$  and  $\text{OPR}_h$ , yielding six free parameters to describe the rotational state of  $\text{H}_2$ . The line-of-sight extinction was treated as a seventh free parameter that was adjusted, along with the other six, to optimize the fit (red and blue dashed curves). The best-fit values are indicated in Figure 4 and are typical of other protostellar outflows observed with Spitzer (e.g., Neufeld et al. 2006).<sup>21</sup>

<sup>21</sup> The positive curvature of the rotational diagram, which we account for with a simple two-component model, suggests that a range of gas temperatures is present (although the temperature distribution need not be bimodal; e.g., Neufeld et al. 2009). The value of  $\text{OPR}_w$ , lying significantly below the value of 3 expected in LTE at temperature  $T_w$ , is suggestive of transient heating in a shock wave; here, the OPR retains a fossil record of its cooler preshock state, there having been insufficient time for it to reach equilibrium (Neufeld et al. 2006, and references therein).

Following Narang et al. (2024), we adopted the KPV5 extinction curve (K. Pontoppidan et al. 2024, in preparation) presented by Chapman et al. (2009), who cited a 2009 unpublished study by K. Pontoppidan for its origin and found that it provided the best fit to the mid-IR extinction and ice features observed in the Spitzer c2d program. The black points indicate the column densities in each rotational state inferred without any extinction correction, while the red and blue points show the values inferred from the extinction-corrected line fluxes. The best-fit extinction optical depth at  $9.7 \mu\text{m}$  is  $\tau_{9.7} = 1.84$ , and other fitting parameters are specified in Figure 4.

To evaluate the sensitivity of our conclusions to our choice of extinction law and aperture size, we have also analyzed the  $\text{H}_2$  rotational emissions within an aperture of radius  $0''.4$  instead of  $0''.8$  and for two additional mid-IR extinction laws that have

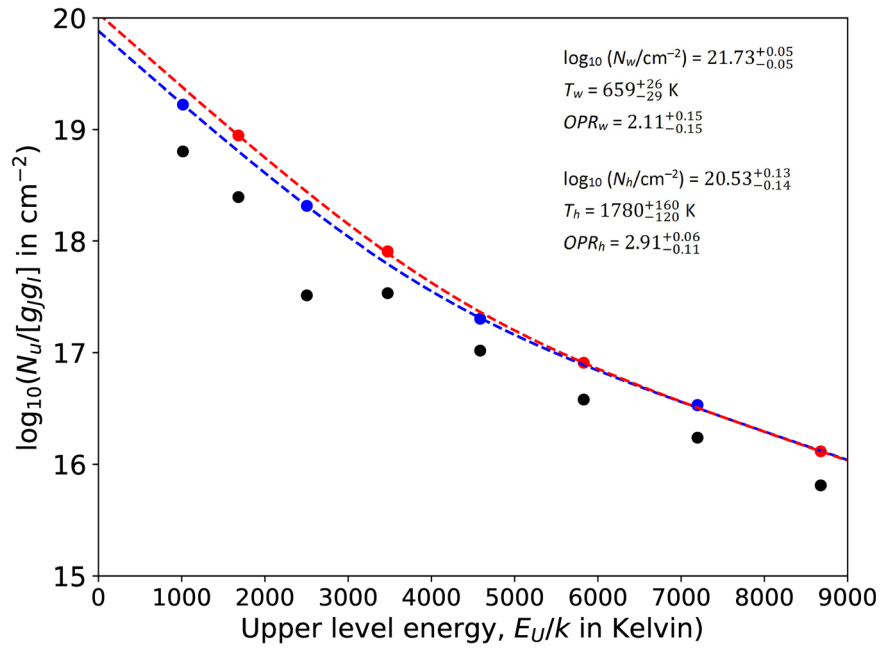


**Figure 4.**  $\text{H}_2$  rotational diagram obtained toward the shocked knots. Black points: no reddening correction. Blue and red points: reddening correction applied. Blue and red dashed lines: best fits to the rotational diagram for ortho- and para- $\text{H}_2$ .

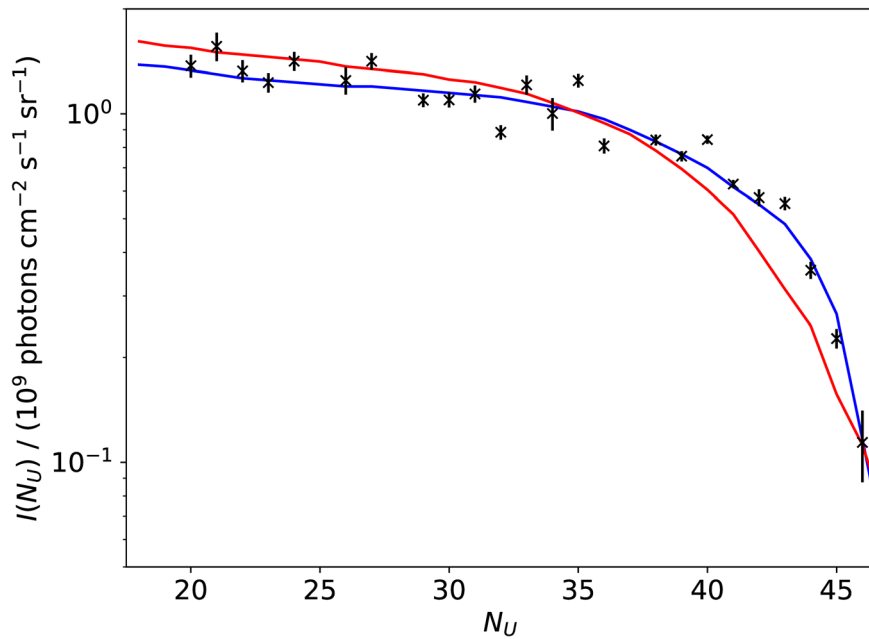


**Figure 5.** OH photon intensity as a function of  $N_U$ . Black points: observed intensities. Also shown are the T21 predictions for  $\text{H}_2\text{O}$  photodissociation by  $\text{Ly}\alpha$  radiation (blue) and by a  $10^4$  K blackbody (red).

appeared in the literature. The results are discussed in Appendix A as they pertain both to the  $\text{H}_2$  analysis discussed above and to the OH analysis discussed below. The relative OH line fluxes favor the KPV5 extinction curve over the alternative extinction laws considered in Appendix A, but the primary conclusions of our study are similar regardless of which mid-IR extinction law or aperture size we adopt.

#### 4. Discussion

##### 4.1. Relative Strengths of the Suprathermal OH Emission Lines

The high signal-to-noise ratio achieved in our observations of suprathermal OH emissions facilitates a demanding test of

theoretical models for their origin. In Figure 5, we plot the mean photon intensity, extinction-corrected with the KPV5 extinction curve, as a function of  $N_U$  (black crosses with bars showing the statistical errors). Here, we excluded the OH transitions with  $N_U = 37, 28,$  and  $25$ , which lie very close to the  $\text{H}_2$  S(3), [Cl I]  $11.33 \mu\text{m}$ , and  $\text{H}_2$  S(2) lines, respectively.

The results are in excellent agreement with the predictions presented in Appendix D of T21, which lists the number of OH line photons expected for each value of  $N_U$  divided by the number of water photodissociations in the  $\tilde{B} - X$  band. These calculations, which rest upon theoretical calculations of the photodissociation dynamics (van Harrevelt & van Hemert 2000) and on experimental measurements (Harich et al. 2000), were

presented by T21 for four different radiation fields. Those expected following water photodissociation by Ly $\alpha$  radiation are shown by the blue curve. There is only one free parameter in this comparison: an overall vertical scaling that is proportional to the photodissociation rate within the beam. If every available UV photon led to water photodissociation via the  $\tilde{B} - X$  band, the required UV photon intensity would be  $I_{UV} = 1.67 \times 10^9$  photons cm $^{-2}$  s $^{-1}$  sr $^{-1}$ . With 24 observed line intensities, the number of degrees of freedom here was  $N_{\text{dof}} = 23$ .

Our analysis here is closely related to that of T21. The only difference is that we present the minimum possible photon intensity,  $I_{UV}$ , that would account for the absolute intensities of the observed OH emissions if every UV photon were absorbed locally by water. This photon intensity is a factor of  $4\pi$  smaller than the quantity  $\Phi$  introduced by T21 and referred to there as the column density of H $_2$ O photodissociated per second.

The observational intensities clearly show systematic errors that are not fully captured by the statistical error bars. Assuming (1) that the predicted curve for Ly $\alpha$  photodissociation (blue) represents the true behavior, (2) that the statistical and systematic errors both have Gaussian distributions with dispersions that may be added in quadrature, and (3) that the fractional systematic error has the same rms,  $\epsilon$ , for all lines, we adjusted  $\epsilon$  to achieve a reduced  $\chi^2$  of unity for the best-fit scaling. The result was  $\epsilon = 0.105$ .

While the blue curve provides an excellent fit to the dependence of the line strengths on  $N_U$ , one aspect of the T21 predictions is in conflict with the observations. Whereas T21 predict roughly equal populations in the symmetric ( $^2\Pi_{3/2}(e)$  and  $^2\Pi_{1/2}(f)$ ) and antisymmetric states ( $^2\Pi_{1/2}(e)$  and  $^2\Pi_{3/2}(f)$ ) of OH, the observations indicate that the symmetric  $A'$  states are strongly favored; indeed, the antisymmetric  $A''$  states are not detected and are at least a factor of  $\sim 10$  less populated than the  $A'$  states. Regardless of the relative rates at which the symmetric and antisymmetric states are populated, the predictions presented in Appendix D of T21 are expected to apply to the total emission in all four  $N_U \rightarrow N_U - 1$  transitions (T21).

This behavior, also noted in the recent paper of Zannese et al. (2024), is in fact entirely consistent with a recent theoretical study of the photodissociation process by Zhou et al. (2015), which indicates a population ratio  $A'/A'' \sim 40$  at the Ly $\alpha$  photon energy (their Figure 7). The astrophysical data thus provide a clear confirmation of the molecular physics. A less-pronounced difference ( $\sim$ a factor of 2) between the line fluxes for the  $A'$  and  $A''$  transitions had previously been measured by Carr & Najita (2014) in Spitzer observations of the protostellar disk in DG Tau. These authors discussed the effect in detail, with reference to two possible origins for OH: photodissociation of H $_2$ O in the  $\tilde{B} - X$  band and chemical pumping following formation via reaction of O( $^1D$ ) with H $_2$ . The larger difference observed in HOPS 370 may indicate that chemical pumping is relatively less important in this source, at least for the  $N_U \geq 20$  transitions discussed here.

The  $N_U$  dependence of the OH line intensities provides information about the ultraviolet radiation field. The red curve in Figure 5 shows the predictions given by T21 for a blackbody radiation field at  $10^4$  K instead of a Ly $\alpha$  radiation field. These tend to overpredict the fluxes for  $N_U < 30$  relative to those for  $N_U > 40$ . For  $\epsilon = 0.105$ , the minimum reduced  $\chi^2$  for this case is  $\chi_{\text{red}}^2 = 2.98$ , implying that the blackbody radiation field is

disfavored at the  $[N_{\text{dof}}(\chi_{\text{red}}^2 - 1)]^{1/2}\sigma = 6.7\sigma$  significance level.

As we did for the H $_2$  emissions discussed in Section 3.3, we have also analyzed the OH emissions within an aperture of radius  $0''.4$  instead of  $0''.8$  and for two additional mid-IR extinction laws that have appeared in the literature. The results are discussed in Appendix A.

#### 4.2. Fraction, $f_w$ , of Ly $\alpha$ Photons Absorbed by Water

The number of Ly $\alpha$  photons available to photodissociate water may be estimated from the Br $\alpha$  flux observed within the circular aperture centered on the shocked knots. In this analysis, we assume a geometry in which the Br $\alpha$  and OH emissions are generated within the shocked knots and viewed directly rather than as a result of scattering, which is favored due their location in distinct shock knots. After degrading the resolution of the Br $\alpha$  map to have the same HPBW as the OH lines, we obtain a value of  $1.4 \times 10^{-14}$  erg cm $^{-2}$  s $^{-1}$  for the Br $\alpha$  flux. If we apply an extinction correction assuming the value of  $\tau_{9.7}$  obtained in Section 3.3 above, this corresponds to an intrinsic flux of  $3.3 \times 10^{-14}$  erg cm $^{-2}$  s $^{-1}$ . As discussed in Appendix B, shock models appropriate for this source predict typical Ly $\alpha$ /Br $\alpha$  luminosity ratios of  $\sim 900$ , a factor of several larger than the Case B recombination ratio because collisional excitation preferentially enhances Ly $\alpha$ .

This would imply a Ly $\alpha$  flux within the aperture of  $3.0 \times 10^{-11}$  erg cm $^{-2}$  s $^{-1}$  or, equivalently, 1.8 photons cm $^{-2}$  s $^{-1}$ . This corresponds to an aperture-averaged intensity of  $3.8 \times 10^{10}$  photons cm $^{-2}$  s $^{-1}$  sr $^{-1}$ , a factor of  $\sim 23$  times as large as the minimum intensity of UV photons needed to account for the OH line fluxes (Section 4.1 above). Therefore, only a fraction  $f_w = 4.3\%$  of the available Ly $\alpha$  photons would need to be absorbed by water to explain the OH emission.

#### 4.3. Interpretation of $f_w$

Ly $\alpha$  photons are unlikely to travel far without being absorbed by dust or water. For Ly $\alpha$  radiation, we obtain a grain absorption cross section per H nucleus of  $\sigma_{\text{abs}}(\text{Ly}\alpha) = 1.9 \times 10^{-21}$  cm $^2$ , adopting the wavelength dependence and albedo given by KPv5; here, the overall scaling was chosen to match the average  $N_{\text{H}}/A_J$  ratio of  $5.6 \times 10^{21}$  cm $^{-2}$  mag $^{-1}$  determined by Vuong et al. (2003) from X-ray absorption observations in several nearby dense clouds.<sup>22</sup> The water photodissociation cross section for Ly $\alpha$  is  $1.53 \times 10^{-17}$  cm $^2$  (Heays et al. 2017, and references therein), and thus the ratio of the water absorption rate to the grain absorption rate for Ly $\alpha$  photons is  $R = 8 \times 10^3 x(\text{H}_2\text{O})$ , where  $x(\text{H}_2\text{O}) = n(\text{H}_2\text{O})/n_{\text{H}}$  is the water abundance relative to H nuclei. The corresponding fraction of Ly $\alpha$  photons absorbed by water is  $f_w = R/(1 + R)$ . The estimate of  $R$  given above is critically dependent on the (poorly known) properties of grains in the outflow. Indeed, it assumes that grains are present in protostellar outflows—as suggested by Cacciapuoti et al. (2024) and references therein—and moreover that their properties are similar to those in the dense interstellar medium. The water abundance required to explain a given value of  $f_w$  scales linearly with the adopted value of  $\sigma_{\text{abs}}(\text{Ly}\alpha)$ .

<sup>22</sup> This scaling is also consistent with the standard  $N_{\text{H}}/A_V$  ratio in diffuse molecular clouds (Bohlin et al. 1978) but yields an  $N_{\text{H}}/A_K$  ratio  $\sim 40\%$  smaller than the average values determined toward diskless pre-main-sequence stars in Serpens and Orion by Winston et al. (2010) and Pillitteri et al. (2013).



If  $f_w = 0.043$  as determined in Section 4.2, and given the grain absorption cross section assumed above, the required water abundance is  $5 \times 10^{-6}$ , amounting to only  $\sim 1\%$  of the gas-phase oxygen abundance.<sup>23</sup> This is the average value,  $\bar{x}(\text{H}_2\text{O})$ , encountered by the Ly $\alpha$  photons as they suffer repeated scatterings with H atoms and execute a random walk prior to their eventual absorption. In the region of Ly $\alpha$  production, the gas is warm ( $T \gtrsim 6000$  K) and/or ionized, and the water abundance will be extremely small. But if the photons escape the region where they are produced without being absorbed by dust, then the water abundance could plausibly exceed  $10^{-4}$  if all oxygen nuclei were driven into gaseous water, and  $R$  could exceed unity. In this scenario, the average water abundance is less meaningful, and the quantity  $f_w$  might primarily reflect the probability that a Ly $\alpha$  photon escapes the warm region where it is originally generated and enters a region where water is abundant. The transfer of Ly $\alpha$  radiation is a complex process (e.g., Neufeld 1990) that can be profoundly affected by velocity shifts associated with shock waves (Neufeld & McKee 1988). We defer a detailed treatment of this process to a future study.

#### 4.4. Lower Limit on the Water Abundance from $\text{H}_2\text{O } \nu_2 = 1 - 0$ Emissions

The rovibrational water line map shown in the upper left panel of Figure 1 shows just one of several dozen emission lines detected in the  $\text{H}_2\text{O } \nu_2 = 1 - 0$  band, which collectively have a total equivalent width of  $\sim 0.120 \mu\text{m}$ . Figure 6 shows the 5.8–7.0 spectral  $\mu\text{m}$  region that is dominated by these emission lines. Unless the density is extraordinarily high ( $n_{\text{H}} \gtrsim 10^9 \text{ cm}^{-3}$ ), these lines are too strong to be produced by collisional excitation. Colored symbols in Figure 6 show the line positions, with stars denoting transitions of ortho-water and plus signs denoting those of para-water. A color code (top left) indicates the minimum energies,  $E_{\text{min}}$ , of the  $\nu = 0$  states that must be pumped radiatively to excite each transition. We note here that  $E_{\text{min}}$  may be smaller than the energy,  $E_L$ , of the lower state of the observed rovibrational transition, since radiative pumping via a given transition may be followed by radiative decay in a different transition of longer wavelength. Roughly 90% of the water emission emerges in transitions that can be pumped radiatively out of the lowest nine rotational states of water (i.e., those with  $J \leq 2$  and  $E/k < 160$  K). This behavior suggests a low rotational temperature within the  $\text{H}_2\text{O } \nu = 0$  state, most likely because the states are subthermally populated, and supports the hypothesis of radiative pumping.

Although a full treatment of the  $\text{H}_2\text{O } \nu_2 = 1 - 0$  emissions is beyond the scope of the present study, we may obtain a lower limit on the mean water abundance,  $x(\text{H}_2\text{O})$ , by assuming that the observed lines are radiatively pumped by radiation from the protostar and that the observed continuum is radiation from the protostar that has been scattered by dust. The equivalent width of the water lines is then

$$W_{\text{H}_2\text{O}} = \sum \frac{F_{\text{H}_2\text{O}}}{F_c} \leq \sum \frac{\int \sigma_{\lambda}(\text{H}_2\text{O}) d\lambda}{\sigma_{\text{sca}}} \left( \frac{n_l(\text{H}_2\text{O})}{n_{\text{H}}} \right), \quad (1)$$

where the sum is taken over all lines in the  $\nu_2 = 1 - 0$  band,  $W_{\text{H}_2\text{O}} = 0.120 \mu\text{m}$  is the total equivalent width (summed over

all  $\text{H}_2\text{O}$  lines),  $F_{\text{H}_2\text{O}}$  is the wavelength-integrated line flux for a given line,  $F_c$  is the continuum flux at the line wavelength,  $\sigma_{\text{sca}}$  is the grain scattering cross section per H nucleus,  $n_l(\text{H}_2\text{O})$  is the number density of water molecules in the lower state, and  $\sigma_{\lambda}(\text{H}_2\text{O})$  is the  $\text{H}_2\text{O}$  cross section for a given rovibrational line (per molecule in the lower state), which has an integral over wavelength  $\lambda$  given by  $A_{ul}\lambda^4/(8\pi c)$ , where  $A_{ul}$  is the spontaneous radiative rate. The equality in Equation (1) applies only if the pumping lines are optically thin.

Because the KPV5 grain model suggests that  $\sigma_{\text{sca}}$  varies only slowly over the band, we may take  $\sigma_{\text{sca}}$  as a constant and approximate the sum of  $A_{ul}\lambda^4 n_l(\text{H}_2\text{O})$  as  $A_{\text{band}} \bar{\lambda}^4 n(\text{H}_2\text{O})$ , where  $A_{\text{band}} = 24 \text{ s}^{-1}$  is the total spontaneous radiation rate for the band and  $\bar{\lambda} = 6.3 \mu\text{m}$  is the average wavelength. Given the grain scattering cross section per H nucleus at  $6.3 \mu\text{m}$  implied by KPV5,  $\sigma_{\text{sca}}(6.3) = 1.2 \times 10^{-23} \text{ cm}^{-2}$ , we then obtain<sup>24</sup>

$$x(\text{H}_2\text{O}) = \frac{n(\text{H}_2\text{O})}{n_{\text{H}}} \geq \frac{8\pi c \sigma_s W_{\text{H}_2\text{O}}}{A_{\text{band}} \bar{\lambda}^4} = 3 \times 10^{-5}. \quad (2)$$

Our water abundance of  $3 \times 10^{-5}$  is a lower limit, and—depending on the water line widths—would likely increase if optical depth effects are included. But even this minimum estimate is a factor of 6 larger than the value needed to yield the inferred value of  $f_w$  (Section 4.3 above). This supports a picture in which most Ly $\alpha$  photons are absorbed by dust in a warm and/or ionized zone very close to where they are created in a fast shock and only a minority escape to the region of significant water abundance that is probed by the water rovibrational emissions. Like the estimate of  $\bar{x}(\text{H}_2\text{O})$  derived in Section 4.3 above, this independent estimate of the minimum water abundance, derived from  $W_{\text{H}_2\text{O}}$ , is also dependent on the grain properties in the outflow; it scales linearly with the value adopted for  $\sigma_{\text{sca}}(6.3)$ . If grains were depleted in the outflow (while maintaining the ratio of  $\sigma_{\text{sca}}(6.3)$  to  $\sigma_{\text{abs}}(\text{Ly}\alpha)$ ), both water abundance estimates would decrease proportionally. Future detailed analyses of the  $\text{H}_2\text{O } \nu_2 = 1 - 0$  spectrum and how it varies spatially will be needed to discriminate between the various mechanisms that release water from ices into the gas phase; these include thermal desorption, sputtering in shocks, and UV photodesorption.

## 5. Summary

We have presented a study of OH in an outflow jet from the HOPS 370 protostar observed with MIRI and NIRSpect as part of the IPA program.

1. We have detected pure rotational, suprathemal OH emissions from the vicinity of the intermediate-mass protostar HOPS 370 (OMC2/FIR3). These emissions are observed from shocked knots in a jet/outflow and originate in states of rotational quantum numbers as high as 46 that possess excitation energies as large as  $E_U/k = 4.65 \times 10^4$  K. Only symmetric  $A'$  states of OH are observed.
2. The relative OH line strengths are entirely consistent with a picture in which the suprathemal OH states are

<sup>23</sup> As noted in Appendix B, our estimate of the required water abundance is quite strongly dependent upon the adopted grain properties: an alternative and widely used grain model in the literature yields a value of only  $1 \times 10^{-6}$ .

<sup>24</sup> A similar argument can be used to determine the CO abundance from observations (Rubinstein et al. 2023) of the CO  $\nu = 1 - 0$  band; here, we obtain a total equivalent width of  $0.140 \mu\text{m}$ , which implies a minimum CO abundance of  $1.1 \times 10^{-4}$  relative to H nuclei.

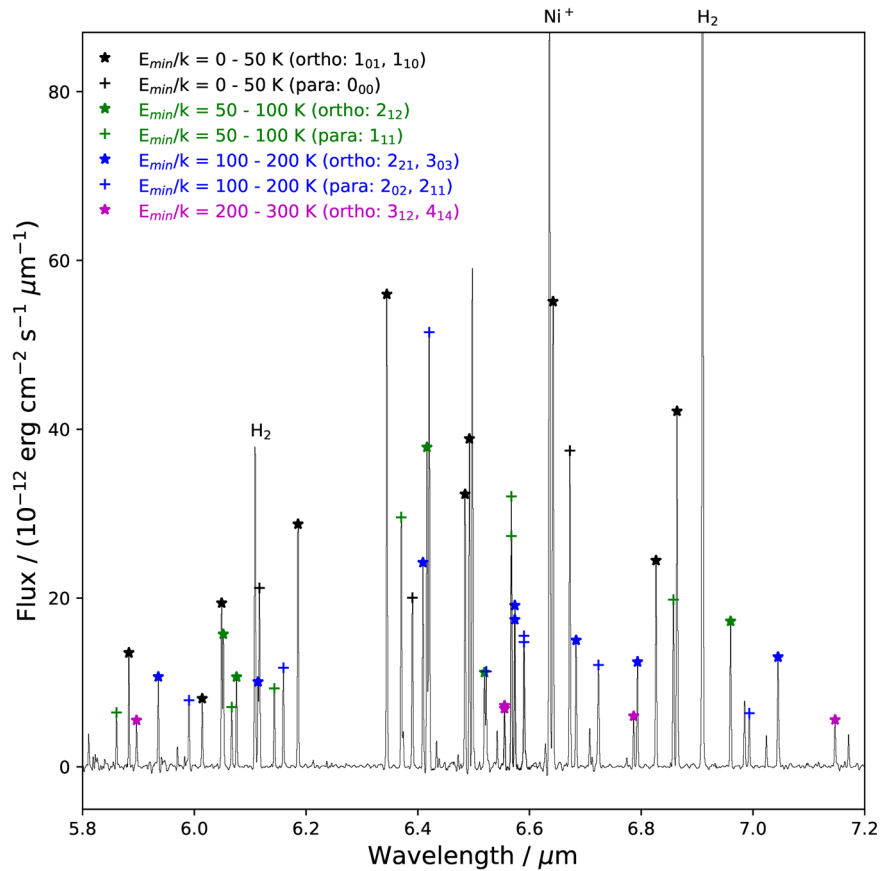


**Figure 6.** Average 5.8–7.0  $\mu\text{m}$  spectrum obtained toward the shocked knots, with rovibrational transitions of ortho- and para-water marked with stars and plus signs.

populated following the photodissociation of water in its  $\bar{B} - X$  band by  $\text{Ly}\alpha$  radiation produced locally by a fast, ionizing shock. Photodissociation by a blackbody radiation field at  $10^4$  K is found to provide a significantly worse fit to the relative OH line strengths.

- Using measurements of the  $\text{Br}\alpha$  flux to estimate the  $\text{Ly}\alpha$  production rate in shocked gas near HOPS 370, we find that  $\sim 4\%$  of the  $\text{Ly}\alpha$  photons are absorbed by water.
- The fraction of  $\text{Ly}\alpha$  photons absorbed by water implies a mean water abundance (relative to H nuclei) in the range  $\bar{x}(\text{H}_2\text{O}) \sim 1\text{--}5 \times 10^{-6}$ , the derived value depending upon the adopted grain properties (Appendix B). This estimate is proportional to the grain absorption cross section assumed at the  $\text{Ly}\alpha$  wavelength (121.6 nm) and represents the average abundance within the region where  $\text{Ly}\alpha$  photons scatter prior to being absorbed by dust or water.
- Assuming that the  $\text{H}_2\text{O } \nu_2$ -band emissions observed from HOPS 370 are radiatively pumped and that the continuum is scattered light, we obtain a minimum water abundance in the range  $x_{\text{min}} = 0.7\text{--}3 \times 10^{-5}$ , the derived value depending upon the adopted grain properties (Appendix A). This minimum value is proportional to the grain scattering cross section assumed at  $6 \mu\text{m}$  and will be exceeded if the pumping lines are optically thick. It is a factor of several larger than  $\bar{x}(\text{H}_2\text{O})$ , suggesting that most  $\text{Ly}\alpha$  photons are absorbed by dust in a warm and/or ionized zone very close to where they are created in a fast shock and that only a minority escape to the region of significant water

abundance that emits the water rovibrational emissions we observe.

- Suprathermal OH emissions promise to help elucidate the processes whereby  $\text{Ly}\alpha$  radiation first escapes from fast shocks and then enters nearby water-rich surroundings where water has been released from grain mantles by radiative heating or slower nondissociative shocks or produced in the gas phase by neutral–neutral reactions that are slow at low temperatures but rapid at the elevated temperatures attained behind shock fronts. Detailed models, beyond the scope of this Letter, will be needed to understand the transfer of  $\text{Ly}\alpha$  radiation and to fully model the rovibrational water emissions observed from HOPS 370.

### Acknowledgments

We thank the referee for a very detailed and helpful review containing multiple suggestions that improved this paper. This work is based on observations made with the NASA/ESA/CSA James Webb Space Telescope. The data were obtained from the Mikulski Archive for Space Telescopes at the Space Telescope Science Institute, which is operated by the Association of Universities for Research in Astronomy, Inc., under NASA contract NAS 5-03127 for JWST. These observations are associated with program No. 1802. D.A.N. was supported by grant SOF08-0038 from USRA. P.M. and H.T. acknowledge support of the Department of Atomic Energy, Government of India, under Project Identification No. RTI 4002. Support for S.F., A.E.R., S.T.M., R.G., W.F., J.G., J.J.T., and

D.W. in program No. 1802 was provided by NASA through a grant from the Space Telescope Science Institute, which is operated by the Association of Universities for Research in Astronomy, Inc., under NASA contract NAS 5-03127. A.C.G. has been supported by PRIN-MUR 2022 20228JPA3A “The path to star and planet formation in the JWST era (PATH)” and by INAF-GoG 2022 “NIR-dark Accretion Outbursts in Massive Young stellar objects (NAOMY).” G.A. and M.O. acknowledge financial support from grants PID2020-114461GB-I00 and CEX2021-001131-S, funded by MCIN/AEI/10.13039/501100011033. Y.-L.Y. acknowledges support from grant-in-aid from the Ministry of Education, Culture, Sports, Science, and Technology of Japan (20H05845, 20H05844, 22K20389) and a pioneering project in RIKEN (Evolution of Matter in the Universe). W.R.M.R. is grateful for support from the European Research Council (ERC) under the European Union’s Horizon 2020 research and innovation program (grant agreement No. 101019751 MOLDISK). All the data presented in this article were obtained from the Mikulski Archive for Space Telescopes (MAST) at the Space Telescope Science Institute. The specific observations analyzed can be accessed via [10.17909/3kky-t040](https://doi.org/10.17909/3kky-t040).

### Appendix A Dependence on Adopted Extinction Curve and Aperture Size

We have evaluated the sensitivity of our conclusions to our choice of extinction law and aperture size. Results are presented in Table 1 for six cases. We considered three different extinction curves—denoted KP (KpV5), WD (Weingartner & Draine 2001, with the modifications described in Draine 2003), and MM (McClure 2009)—and two different aperture radii (0".8 and 0".4, denoted by 1 and 2). The standard model, adopted in the main text, is KP1 (KpV5 extinction curve with the 0".8 radius aperture).

Different rows in Table 1 show the values obtained for key parameters for all six cases. The first row lists the optical depth at 9.7  $\mu\text{m}$ ,  $\tau_{9.7}$ , derived from our fit to the H<sub>2</sub> lines. It ranges

from 1.53 to 3.12, with the MM extinction law (which is significantly less dominated by the silicate peak) requiring the largest  $\tau_{9.7}$  and the WD extinction law requiring the smallest, but it shows very little variation with the adopted aperture size. The second row lists  $I_{\text{UV}}$ , the required UV photon intensity if every available UV photon led to water photodissociation via the  $\tilde{B} - X$  band. In determining  $I_{\text{UV}}$ , the OH lines were extinction-corrected using the specified extinction curve and the corresponding value of  $\tau_{9.7}$ , and Ly $\alpha$  was assumed to be responsible for water photodissociation. As discussed in Section 4.1, we assumed equal fractional systematic errors,  $\epsilon$ , for each OH flux measurement and adjusted  $\epsilon$  to yield a reduced  $\chi^2$  of unity when comparing case KP1 and KP2 fluxes with the predictions for Ly $\alpha$  photodissociation. The third row lists the reduced  $\chi^2$  obtained for each of the six cases. The fourth row lists the corresponding values obtained for a 10<sup>4</sup> K blackbody radiation field instead of Ly $\alpha$ . The fifth and sixth rows indicate the significance with which each case is disfavored relative to KP1 or KP2 with photodissociation by Ly $\alpha$ . The values plotted here indicate that (1) the KP extinction law yields a significantly better fit to the data than either WD or MM, and (2) for any extinction curve, assuming photodissociation by Ly $\alpha$  radiation yields a significantly better fit to the data than does assuming photodissociation by a 10<sup>4</sup> K blackbody.

The seventh row in Table 1 lists the extinction-corrected (ec) Br $\alpha$  intensity,  $I(\text{Br}\alpha)_{\text{ec}}$ , for each of the six cases. The next row lists the corresponding values of  $f_w$ , the fraction of Ly $\alpha$  photons absorbed by dust. The quantity  $f_w$  was computed for an assumed Ly $\alpha$ /Br $\alpha$  ratio of 900 (see Appendix B) and is proportional to  $I_{\text{UV}}/I(\text{Br}\alpha)_{\text{ec}}$ . Although  $I_{\text{UV}}$  varies over a factor of 4–5 as different extinction curves are adopted,  $f_w$  varies by less than a factor of 2. This is because there is some degree of cancellation between the effects on  $I_{\text{UV}}$  and  $I(\text{Br}\alpha)_{\text{ec}}$ . The MM extinction curve, for example, requires a significantly larger  $\tau_{9.7}$  leading to a significantly larger  $I_{\text{UV}}$ , but because the opacity is less strongly peaked at the silicate feature,  $I(\text{Br}\alpha)_{\text{ec}}$  also increases by a factor of 2.

**Table 1**  
Results for Different Extinction Laws and Aperture Sizes

Row	Quantity	KP1 0".8	WD1 0".8	MM1 0".8	KP2 0".4	WD2 0".4	MM2 0".4
1	$\tau_{9.7}$	1.84	1.53	3.12	1.85	1.53	3.05
2	$I_{\text{UV}}$ ( $10^9$ photons $\text{cm}^{-2}$ $\text{s}^{-1}$ $\text{sr}^{-1}$ )	1.67	1.10	5.11	3.75	2.42	1.07
3	Reduced $\chi^2$ (with respect to Ly $\alpha$ model)	1.00	1.63	1.55	1.00	2.65	2.33
4	Reduced $\chi^2$ (with respect to 10 <sup>4</sup> K blackbody model)	2.98	6.13	4.60	3.74	8.40	7.30
5	Significance <sup>a</sup> (for Ly $\alpha$ model)	0.0 $\sigma$	4.4 $\sigma$	3.6 $\sigma$	0.0 $\sigma$	6.2 $\sigma$	5.5 $\sigma$
6	Significance <sup>a</sup> (for 10 <sup>4</sup> K blackbody model)	6.7 $\sigma$	10.9 $\sigma$	9.1 $\sigma$	7.9 $\sigma$	13.0 $\sigma$	12.0 $\sigma$
7	$I(\text{Br}\alpha)_{\text{ec}}$ ( $10^{-3}$ erg $\text{cm}^{-2}$ $\text{s}^{-1}$ $\text{sr}^{-1}$ )	0.71	0.72	3.64	1.49	1.52	7.22
8	$f_w$	0.043	0.028	0.025	0.046	0.029	0.027
9	$\sigma_{\text{abs}}(\text{Ly}\alpha)$ ( $10^{-21}$ $\text{cm}^2$ )	1.73	0.70	N/A	1.73	0.70	N/A
10	$\bar{x}(\text{H}_2\text{O})$	$5.1 \times 10^{-6}$	$1.3 \times 10^{-6}$	N/A	$5.1 \times 10^{-6}$	$1.3 \times 10^{-6}$	N/A
11	$\sigma_{\text{sca}}(6.3)$ ( $10^{-23}$ $\text{cm}^2$ )	1.26	0.29	N/A	1.26	0.29	N/A
12	$W_{\text{H}_2\text{O}}$ ( $\mu\text{m}$ )	0.120	0.120	0.120	0.168	0.168	0.168
13	$x_{\text{min}}(\text{H}_2\text{O})$	$3.0 \times 10^{-5}$	$7.0 \times 10^{-6}$	N/A	$4.2 \times 10^{-5}$	$1.0 \times 10^{-5}$	N/A

**Note.**

<sup>a</sup> Significance with which a given model and extinction curve are disfavored relative to the model with Ly $\alpha$  photodissociation and the KP extinction curve.

The conclusions of our sensitivity analysis are that (1) similar results are obtained for both aperture sizes; (2) as the origin of the suprathermal OH emissions, water photodissociation by  $\text{Ly}\alpha$  radiation is robustly favored over photodissociation by a  $10^4$  K blackbody; (3) the KPV5 extinction is favored over the other two extinction laws considered here; and (4) the parameter  $f_w$  lies in the range 2.6%–4.3% for any of the extinction laws we considered.

The ninth–thirteenth rows are relevant to the water abundances discussed in Sections 4.3 and 4.4. Here, not only is the relative extinction at different wavelengths of relevance but so is the grain albedo and the ratio of extinction to column density,  $N_{\text{H}}$ . Both of these parameters are available for the KP and WD extinction laws but not for MM. The ninth row lists the grain absorption cross section per H nucleus,  $\sigma_{\text{abs}}(\text{Ly}\alpha)$ , given by each extinction law. The average water abundance,  $\bar{x}(\text{H}_2\text{O})$ , needed to account for  $f_w$  is listed in the tenth row (see Section 4.3). The eleventh row lists the grain scattering cross section,  $\sigma_{\text{sca}}(6.3)$ , needed for the analysis presented in Section 4.4, while the twelfth row lists the total  $\nu_2 = 1 - 0$  equivalent width,  $W_{\text{H}_2\text{O}}$ , for each aperture. The resultant minimum water abundances,  $x_{\text{min}}(\text{H}_2\text{O})$  (see Section 4.3), are given in the thirteenth row.

The results presented here for  $\bar{x}(\text{H}_2\text{O})$  and  $x_{\text{min}}(\text{H}_2\text{O})$  are clearly more sensitive to uncertainties in the dust properties. Nevertheless, the conclusion that  $\bar{x}(\text{H}_2\text{O}) < x_{\text{min}}(\text{H}_2\text{O})$  appears to be robust, with the implications for  $\text{Ly}\alpha$  radiative transfer discussed in Section 4.4.

## Appendix B Shock Model Predictions for $\text{Ly}\alpha/\text{Br}\alpha$

We have used the publicly available MAPPINGS V shock model (Sutherland & Dopita 2017; Sutherland et al. 2018) to estimate the  $\text{Ly}\alpha/\text{Br}\alpha$  luminosity ratio within the shocked region where suprathermal OH emissions were detected. The upper states of these lines may be populated both following

recombination of  $\text{H}^+$  and by direct collisional excitation of neutral hydrogen from the ground state. The  $\text{Ly}\alpha/\text{Br}\alpha$  ratio can significantly exceed the Case B recombination value of  $\sim 300$ , particularly for lower-velocity shocks where collisional excitation is most important, so the use of shock model predictions is important here.

We ran a grid of models with preshock densities,  $n_0$ , spanning the range  $10^{-1}$ – $10^{5.5}$  H nuclei per  $\text{cm}^{-3}$  in steps of 0.1 dex and with shock velocities,  $v_s$ , spanning the range 30–220  $\text{km s}^{-1}$  in steps of 5  $\text{km s}^{-1}$ . The preshock ionization state was determined self-consistently. The preshock magnetic field was taken as  $0.5(n_0/\text{cm}^{-3})^{1/2} \mu\text{G}$ , and undepleted solar abundances were adopted. The collision strengths for [Fe II] fine-structure transitions were updated to the values given in the recent study of Tayal & Zatsarinny (2018).


Figure 7 shows contours of the predicted  $\text{Ly}\alpha/\text{Br}\alpha$  luminosity ratio in the plane of  $v_s$  and  $\log_{10}n_0$ . Here, the red, cyan, and blue contours show where the  $\text{Ly}\alpha/\text{Br}\alpha$  ratio is predicted to be 1000, 1500, and 2000, and black contours show intermediate values spaced by 100. The [Ne III] 15.6  $\mu\text{m}$  to [Ne II] 12.8  $\mu\text{m}$  flux ratio is an excellent tracer of shock velocity. The observed, extinction-corrected value of 0.026 is obtained for shock parameters lying along the locus marked with the green solid curve. The green band indicates the region where the predicted value lies within a factor of 1.5 of that observed, with the dotted/dashed boundaries applying to larger/smaller line ratios. As a probe of the preshock density, we have considered the [Fe II] 17.9  $\mu\text{m}$  to [Fe II] 5.3  $\mu\text{m}$  flux ratio, which has an observed extinction-corrected value of 4.17. The magenta curves and magenta band represent analogous results for the [Fe II] line ratio. The constraint on density is less tight, as indicated by the width of the magenta band, and must be considered less reliable because recent independent estimates of the collision strengths show significant differences. Nevertheless, the intersection of the green and magenta solid lines suggest that the  $\text{Ly}\alpha/\text{Br}\alpha$  ratio of 900 is consistent with these

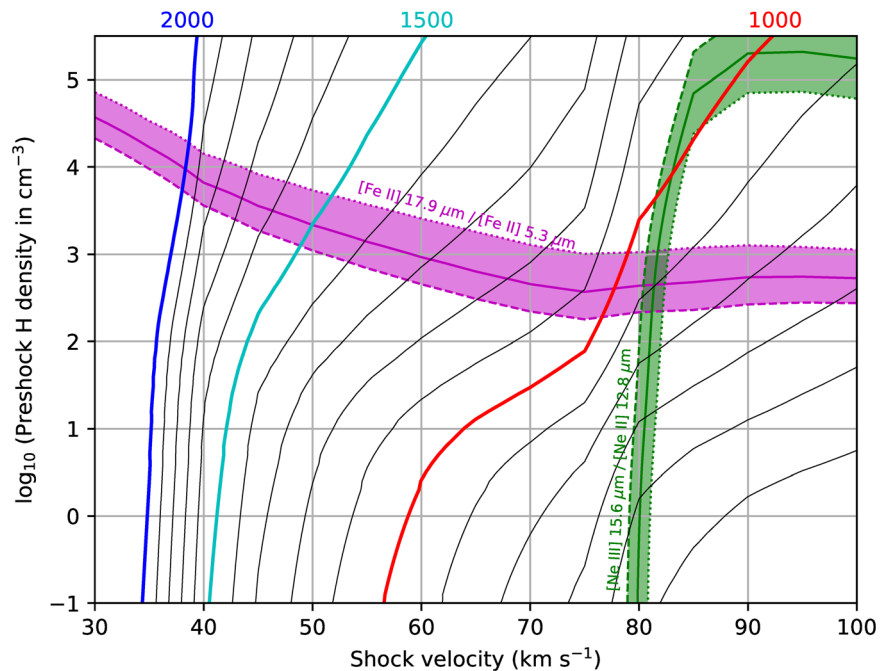


**Figure 7.** Contours of the predicted  $\text{Ly}\alpha/\text{Br}\alpha$  luminosity ratio in the plane of  $v_s$  and  $\log_{10}n_0$ . Red, cyan, and blue contours:  $\text{Ly}\alpha/\text{Br}\alpha = 1000, 1500,$  and  $2000$ . Green band: region where the predicted [Ne III] 15.6  $\mu\text{m}$  to [Ne II] 12.8  $\mu\text{m}$  flux ratio lies within a factor of 1.5 of that observed. Magenta band: region where the predicted [Fe II] 17.94  $\mu\text{m}$  to [Fe II] 5.34  $\mu\text{m}$  flux ratio lies within a factor of 1.5 of that observed.

diagnostic line ratios. For any preshock density in the range  $10^2$ – $10^5$   $\text{cm}^{-3}$ , the [Ne III]  $15.6\ \mu\text{m}$  to [Ne II]  $12.8\ \mu\text{m}$  flux ratio *alone* suggests a  $\text{Ly}\alpha/\text{Br}\alpha$  ratio in the range of 700–1050.

### ORCID iDs

David A. Neufeld  <https://orcid.org/0000-0001-8341-1646>  
 P. Manoj  <https://orcid.org/0000-0002-3530-304X>  
 Himanshu Tyagi  <https://orcid.org/0000-0002-9497-8856>  
 Mayank Narang  <https://orcid.org/0000-0002-0554-1151>  
 Dan M. Watson  <https://orcid.org/0000-0001-8302-0530>  
 S. Thomas Megeath  <https://orcid.org/0000-0001-7629-3573>  
 Ewine F. Van Dishoeck  <https://orcid.org/0000-0001-7591-1907>  
 Robert A. Gutermuth  <https://orcid.org/0000-0002-6447-899X>  
 Thomas Stanke  <https://orcid.org/0000-0002-5812-9232>  
 Yao-Lun Yang  <https://orcid.org/0000-0001-8227-2816>  
 Adam E. Rubinstejn  <https://orcid.org/0000-0001-8790-9484>  
 Guillem Anglada  <https://orcid.org/0000-0002-7506-5429>  
 Henrik Beuther  <https://orcid.org/0000-0002-1700-090X>  
 Alessio Caratti o Garatti  <https://orcid.org/0000-0001-8876-6614>  
 Neal J. Evans, II  <https://orcid.org/0000-0001-5175-1777>  
 Samuel Federman  <https://orcid.org/0000-0002-6136-5578>  
 William J. Fischer  <https://orcid.org/0000-0002-3747-2496>  
 Joel Green  <https://orcid.org/0000-0003-1665-5709>  
 Pamela Klaassen  <https://orcid.org/0000-0001-9443-0463>  
 Leslie W. Looney  <https://orcid.org/0000-0002-4540-6587>  
 Mayra Osorio  <https://orcid.org/0000-0002-6737-5267>  
 Pooneh Nazari  <https://orcid.org/0000-0002-4448-3871>  
 John J. Tobin  <https://orcid.org/0000-0002-6195-0152>  
 Łukasz Tychoniec  <https://orcid.org/0000-0002-9470-2358>  
 Scott Wolk  <https://orcid.org/0000-0002-0826-9261>

### References

Bohlin, R. C., Savage, B. D., & Drake, J. F. 1978, *ApJ*, 224, 132  
 Brooke, J. S. A., Bernath, P. F., Western, C. M., et al. 2016, *JQSRT*, 168, 142

Brunken, N. G. C., Rocha, W. R. M., van Dishoeck, E. F., et al. 2024, arXiv:2402.04314  
 Cacciapuoti, L., Testi, L., Podio, L., et al. 2024, *ApJ*, 961, 90  
 Carr, J. S., & Najita, J. R. 2014, *ApJ*, 788, 66  
 Chapman, N. L., Mundy, L. G., Lai, S.-P., et al. 2009, *ApJ*, 690, 496  
 Christiaens, V., Gonzalez, C., Farkas, R., et al. 2023, *JOSS*, 8, 4774  
 Federman, S., Megeath, S. T., Rubinstein, A. E., et al. 2023, arXiv:2310.03803  
 Furlan, E., Fischer, W. J., Ali, B., et al. 2016, *ApJS*, 224, 5  
 Gomez Gonzalez, C. A., Wertz, O., Absil, O., et al. 2017, *AJ*, 154, 7  
 González-García, B., Manoj, P., Watson, D. M., et al. 2016, *A&A*, 596, A26  
 Harich, S. A., Hwang, D. W. H., Yang, X., et al. 2000, *JChPh*, 113, 10073  
 Heays, A. N., Bosman, A. D., & van Dishoeck, E. F. 2017, *A&A*, 602, A105  
 Jones, O. C., Álvarez-Márquez, J., Sloan, G. C., et al. 2023, *MNRAS*, 523, 2519  
 Kounkel, M., Covey, K., Suárez, G., et al. 2018, *AJ*, 156, 84  
 Law, D. R., Morrison, J. E., Argyriou, I., et al. 2023, *AJ*, 166, 45  
 Manoj, P., Watson, D. M., Neufeld, D. A., et al. 2013, *ApJ*, 763, 83  
 Megeath, S. T., Gutermuth, R., Muzerolle, J., et al. 2012, *AJ*, 144, 192  
 Megeath, T., Anglada, G., Atmagulov, P., et al. 2021, JWST Proposal. Cycle, 1, 1802  
 Narang, M., Manoj, P., Tyagi, H., et al. 2024, *ApJL*, 962, L16  
 Nazari, P., Cheung, J. S. Y., Ferrer Asensio, J., et al. 2024, arXiv:2401.04760  
 Neufeld, D. A. 1990, *ApJ*, 350, 216  
 Neufeld, D. A., & McKee, C. F. 1988, *ApJL*, 331, L87  
 Neufeld, D. A., Melnick, G. J., Sonnentrucker, P., et al. 2006, *ApJ*, 649, 816  
 Neufeld, D. A., Nisini, B., Giannini, T., et al. 2009, *ApJ*, 706, 170  
 Osorio, M., Díaz-Rodríguez, A. K., Anglada, G., et al. 2017, *ApJ*, 840, 36  
 Pillitteri, I., Wolk, S. J., Megeath, S. T., et al. 2013, *ApJ*, 768, 99  
 Rubinstein, A. E., Tyagi, H., Nazari, P., et al. 2023, arXiv:2312.07807  
 Sato, A., Takahashi, S., Ishii, S., et al. 2023, *ApJ*, 944, 92  
 Sutherland, R., Dopita, M., Binette, L., et al., 2018 MAPPINGS V: Astrophysical plasma modeling code, Astrophysics Source Code Library, ascl:1807.005  
 Sutherland, R. S., & Dopita, M. A. 2017, *ApJS*, 229, 34  
 Tabone, B., van Hemert, M. C., van Dishoeck, E. F., et al. 2021, *A&A*, 650, A192  
 Tappe, A., Lada, C. J., Black, J. H., et al. 2008, *ApJL*, 680, L117  
 Tayal, S. S., & Zatsarinny, O. 2018, *PhRvA*, 98, 012706  
 Tobin, J. J., Sheehan, P. D., Reynolds, N., et al. 2020, *ApJ*, 905, 162  
 van Harrelvelt, R., & van Hemert, M. C. 2000, *JChPh*, 112, 5787  
 Vuong, M. H., Montmerle, T., Grosso, N., et al. 2003, *A&A*, 408, 581  
 Winston, E., Megeath, S. T., Wolk, S. J., et al. 2010, *AJ*, 140, 266  
 Zannese, M., Tabone, B., Habart, E., et al. 2024, *NatAs*, *Advanced Online Publication*  
 Zhou, L., Xie, D., & Guo, H. 2015, *JChPh*, 142, 124317